Six-probe scintillator dosimeter for treatment verification in HDR-brachytherapy

Mathieu Gonod[1], Miguel Angel Suarez[2], Carlos Chacon Avila[2], Vage Karakhanyan[2], Clément Eustache[2], Samir Laskri[3], Julien Crouzilles[3], Jean-François Vinchant[3], Léone Aubignac[1] and Thierry Grosjean[2]
[1]Centre Georges François Leclerc (CGFL) - Dijon, France
[2]University of Franche-Comté, CNRS, FEMTO-ST Institute, UMR 6174, Besançon, France
[3]SEDI-ATI Fibres Optiques, 8 Rue Jean Mermoz, 91080 Évry-Courcouronnes, France

Version typeset November 15, 2024

Author to whom correspondence should be addressed. email: thierry.grosjean@univ-fcomte.fr

Abstract

Background: *In vivo* dosimetry (IVD) is gaining interest for treatment delivery verification in HDR-brachytherapy. Time resolved methods, including source tracking, have the ability both to detect treatment errors in real time and to minimize experimental uncertainties. Multiprobe IVD architectures holds promise for simultaneous dose determinations at the targeted tumor and surrounding healthy tissues while enhancing measurement accuracy. However, most of the multiprobe dosimeters developed so far either suffer from compactness issues or rely on complex data post-treatment.

Purpose: We introduce a novel concept of a compact multiprobe scintillator detector and demonstrate its applicability in HDR-brachytherapy. Our fabricated seven-fiber probing system is sufficiently narrow to be inserted in a brachytherapy needle or in a catheter.

Methods: Our multiprobe detection system results from the parallel implementation of six miniaturized inorganic Gd_2O_2S:Tb scintillator detectors at the end of a bundle of seven fibers, one fiber is kept bare to assess the stem effect. The resulting system, which is narrower than 320 microns, is tested with a MicroSelectron 9.14 Ci Ir-192 HDR afterloader, in a water phantom. The detection signals from all six probes are simultaneously read with a sCMOS camera (at a rate of 0.06 s). The camera is coupled to a chromatic filter to cancel Cerenkov signal induced within the fibers upon exposure. By implementing an aperiodic array of six scintillating cells along the bundle axis, we first determine the range of inter-probe spacings leading to optimal source tracking accuracy (first tracking method). Then, three different source tracking algorithms involving all the scintillating probes are tested and compared. In each of these four methods, dwell positions are assessed from dose measurements and compared to the treatment plan. Dwell time is also determined and compared to the treatment plan.

Results: The optimum inter-probe spacing for an accurate source tracking ranges from 15 mm to 35 mm. The optimum detection algorithm consists of adding the readout signals from all detector probes. In that case, the error to the planned dwell positions is of 0.01 ± 0.14 mm and 0.02 ± 0.29 mm at spacings between the source and detector axes of 5.5 and 40 mm, respectively. Using this approach, the average deviations to the expected dwell time are of -0.006±0.009 s and -0.008 ± 0.058 s, at spacings between source and probe axes of 5.5 mm and 20 mm, respectively.

Conclusions: Our six-probe Gd_2O_2S:Tb dosimeter coupled to a sCMOS camera can perform time-resolved treatment verification in HDR brachytherapy. This detection system of high spatial and temporal resolutions (0.25 mm and 0.06s, respectively) provides a precise information on the treatment delivery via a dwell time and position verification of unmatched accuracy.

This is a sample note.

Contents

I. Introduction

High dose rate brachytherapy (HDR-BT) is a standard modality in cancer treatment which offers advantages of highly localized dose distributions and minimum number of treatment fractions.[1,2,3,4]. To ensure that the planned dose is properly delivered, time-resolved in vivo dosimetry (IVD) has been proposed for monitoring treatments and detecting errors[5,6,7,8,9]. Among time-resolved IVD approaches, optical fibers coupled to scintillators have shown promise in time-resolved verification of the dose rate[10,11,12,13,14,15,16,17], as well as dwell position and dwell time monitoring of a stepping radioactive source[7,15,18,19,20].

IVD in multiprobe architectures has recently attracted attention for its ability to increase the spatial extent of treatment monitoring to volumes including the targeted tumor and surrounding healthy tissues. By use of individual detectors in various parallel catheters, Wang et al.[21] and Guiral et al.[22] performed extended source tracking along the source catheter. Cartwright et al[23] implemented a source tracking with an array of 16 plastic scintillator dosimeters embedded in a 20 mm-diameter rectal applicator. However, the acquisition rate of the detector was limited to 1 s, short dwell times of the source could not be assessed. Moreover, the diameter of the resulting multiprobe dosimeter in the centimeter range limits its field of application in BT. Therriault-Proulx et al.[24] developed a three-probe plastic scintillator detector sufficiently narrow to be inserted within a BT needle or catheter, thereby making multiprobe tracking applicable in a broader range of BT. Because they involve one-millimeter outer diameter fibers, the three scintillator probes were engineered on the same fiber to be insertable into a BT needle or catheter. In this specific setup, where the luminescence from all three scintillators travels through the same physical path within the fiber, the optical signals are entangled at the fiber output. By analyzing the optical signal with a spectrometer, dosimetry has been successfully demonstrated with a detection rate as large as 3 seconds. A recent study has introduced a hyper-spectral optical detection system enabling time-resolved dose rate monitoring as well as dwell position and dwell time verification with such a fiber detector[19,25]. To determine the dose received by each individual scintillator from the detected optical signals, a calibration process based on the AAPM TG-43 dose parameters[26] has been implemented[25]. The detected optical signals were combined in a 4×4 linear equation system to obtain a detector overall response that is free from the stem effect[25,27]. With this system, triangulation approaches for source tracking were demonstrated.

In this paper, we use the miniaturized scintillator detector (MSD) approach[28,29,30] to demonstrate a seven-channel multiprobe detector that is narrow enough to perform time-resolved treatment monitoring within a single BT needle or catheter. Our 320-micron outer diameter fiber detector consists of 6 scintillating probes and a bare test-fiber, engineered at the end of a narrow seven-fiber bundle. The parallel measurement of the seven optical signals at the bundle output with a sCMOS camera avoids inter-probe cross-talk, i.e., signal entanglement at the bundle output. As a result, the calibration of our multiprobe detector does not require the use of the AAPM TG-43 algorithm. Moreover, Cerenkov signal is simply removed by positioning a bandpass filter in front of the camera. Each MSD of the detection system ensures minimum volume averaging within the steep dose gradients of BT sources, leading to unmatched source tracking performances in space and time.

II. Material and Methods

II.A. Multiprobe system

The multiprobe detector (MPD) shown in Fig. 1(b) involves a 10-meter-long bundle of seven biocompatible fibers arranged in a hexagonal lattice (cf. Fig. 1(a); fabricated by SEDI-ATI). Each fiber is of 80-micron outer diameter (50-micron core diameter) and is covered with a 5-micron-thick polyimide protective coating. The total width of the bundle is of 270 microns. Each fiber tip is tapered in the form of a leaky-wave nano-optical antenna[28,31] aimed at improving the transfer of the X-ray excited luminescence from the scintillators to the fiber. Scintillating powder (Gd_2O_2S:Tb) is locally attached to the tapered tip of six of the seven fibers to form the probes P1-P4, P6 and P7 (see Fig. 1(b)). Gd_2O_2S:Tb is chosen as the scintillating material owing to its high scintillation efficiency, stability, linearity and fast temporal response[32,33,34] and with very low sensitivity to temperature (in the range of 15°-40°)[35,36]. This inorganic scintillator shows an energy dependence[30] that need to be corrected if a direct dose rate measurement, rather than a source tracking, is targeted. The last bare fiber, labelled as P5, is used to evaluate the level of spurious Cerenkov signal generated within fibers upon irradiation. The overall fabrication process is detailed in Refs.[29,30]. The MPD is locally enlarged to diameters around 320 microns by the presence of the scintillating cells (see Fig. 1(c)). The scintillation cells forming the six parallel probes are shown in Fig. 1(d). The scintillation volume varies from 0.008 mm^3 (P1) to 0.009 mm^3 (P3), due to slight imperfections in our fabrication process, in terms of reproducibility. Four different inter-probe spacings along the bundle axis are defined by adapting the length of each optical fiber of the bundle. P1 and P2, P2 and P3, and P4 and P6 are spaced by Δ, 2Δ, and 4Δ, respectively, where $\Delta = 5$ mm, whereas P3 and P4 as well as P6 and P7 are both spaced by 1.7Δ. Interprobe spacings are defined with an accuracy of 0.3 mm. Measurements where realized by positioning the MPD onto a calibrated motorized stage coupled to a binocular equipped with a crosshair. The fiber bundle is positioned within a black 0.9-mm hytrel cladding to minimize collection of the background light from the test room. This opaque shield stops about 10 cm before the first probe P1 so that all six probes plus the bare fiber are directly in contact to the water phantom. To avoid contribution from external spurious light, the experiments are carried out in the dark. In addition, an opaque cover is used to protect the water phantom from residual room light.

II.B. Optical readout

The optical signals at the end of the MPD are simultaneously recorded with a sCMOS camera (Andor Technology, Zyla 4.2 model) whose maximum detection yield spectrally matches the emission of the Gd_2O_2S:Tb material. A 35 mm camera objective (Fujinon HF35SA) is positioned in front of the camera to image the bare output face of the fiber bundle at a rate of 0.06 s. Prior to acquisitions, we define seven regions of interest (ROI) tightly enclosing the seven light spots that are observable in the image (one spot per probe, see the green circles in Fig. 1(e) delimiting the ROIs). Our code, developed under Labview environment, automatically defines the ROIs as 16-pixel diameter disks centered with respect to the maximum signal. The image pixels located within each ROI are integrated to obtain seven detection signals sampled at 0.06 s. A chromatic filter (544/24 nm band pass filter from Semrock) is positioned in front of the camera to filter out the spurious Cerenkov signal (stem effect) generated in the fibers upon exposure.[29].

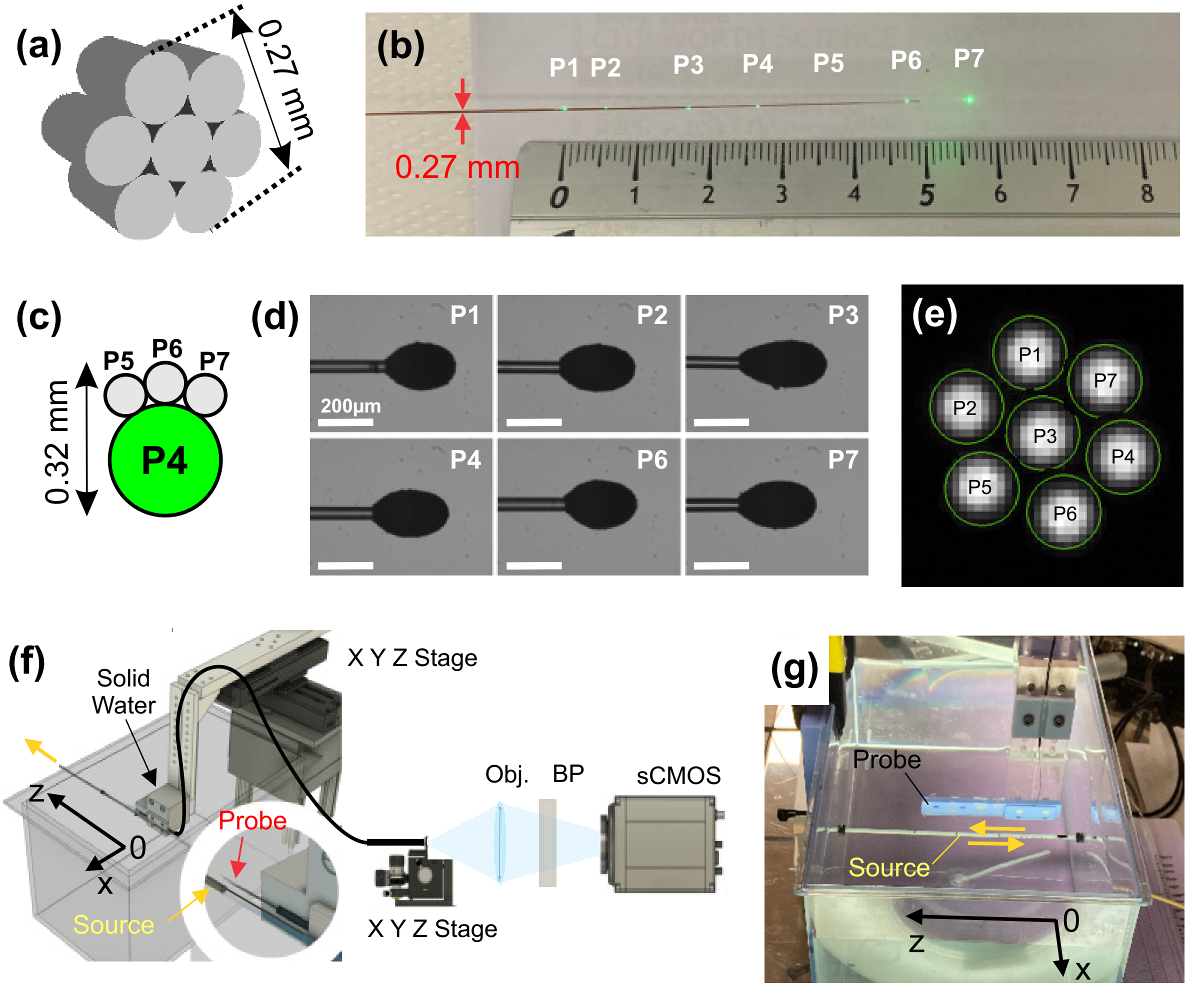

Figure 1: (a) Schematic of the bundle of 7 fibers arranged in an hexagonal lattice. (b) Photograph of the multiprobe detector. Green laser light is coupled to the free bare facet of the fiber bundle to identify in the image the six scintillation cells (six green spots are observed due to light scattering of the fiber modes by the scintillators). (c) Schematic of a cross-section of the MPD at the location of probe P4 (cf. (b)). The green and gray disks represent the cross-sections of the scintillating cell and fibers, respectively. (d) Magnified optical images of the six scintillation cells at the end of the fiber bundle. (e) Image of the bare face of the fiber bundle by the sCMOS camera when white light is projected onto the seven probes. (f) Schematics of the experimental setup involving a water tank, the multiprobe detector positioned onto a 2D motorized stage and a photometer based on a sCMOS camera coupled to an objective (Obj.) and a band-pass filter (BP). (g) Photograph of the experimental setup.

II.C. Brachytherapy system

A MicroSelectron afterloader with a 9.14 Ci Ir-192 HDR source (Air kerma strength of 37309 U) is used for irradiation.

II.D. Phantom

The probe characterization is conducted in a 40x30x30 cm^3 water tank. The source catheter crosses the tank widthwise (Figs. 1(f) and (g)). During experiments, temperature in the water phantom varies from 17° to 19° (temperature assessment with a thermometer before and after the experiments). The MPD is fixed to a solid-water holder that is attached to a 2D translation stage via a plastic adaptor (Figs.1(f) and (g)). The fiber probe is set parallel to the source catheter. A coordinate frame of the set-up is defined so that the origin of the frame coincides with the scintillators of the proximal probe $P1$. The source-probe spacing along the (0x) and (0z) axes is determined with the motorized stage and the afterloader, respectively.

II.E. Detector calibration

The MPD is calibrated along seven lines parallel to the (0z)-axis. These lines are spaced by 5.5, 8, 10, 15, 20, 30 and 40 mm (along (0x)) from the axis of the source catheter. First, the MPD is positioned at the desired source-probe inter-catheter spacing x with the motorized stage. Then, the source is displaced along the fixed source catheter by 2.5-mm steps. The calibration curves are obtained by integrating 165 images per source position. An interpolation (performed with the ”interp” function of Matlab software) is applied to the measured profiles to obtain a 0.1-mm sampling rate. During calibration, we verify with the scintillator-free fiber probe P5 that no optical signal (stem effect) is detected with the chromatic filter positioned in front of the camera.

The signal-to-noise ratio (SNR) of the six scintillating probes forming the detector is assessed at the dwell positions corresponding to the maxima of all the above-mentioned calibration curves, at the seven source-probe spacings x ranging from 5.5 mm to 40 mm. The SNR is the average amplitude of the signal divided by its standard deviation.

II.F. Dwell position and dwell time verification

II.F.1. Measurements

To test the MPD, an irradiation protocol consisting of 40 dwell positions is applied for each value of source-probe spacing along $(0x)$. The dwell positions are spaced by 2.5 mm and the dwell time is fixed to 10 s. Note that 2.5-mm is the minimum displacement step allowed by our afterloader. With a source tracking accuracy of 0.023 ± 0.077 mm[30], our sub-millimeter scintillating probes are suitable to accurately track shorter sources steps (e.g., 1 mm steps). The dwell time value has been fixed to 10s for a direct comparison of our source-tracking results with those of Linares et al.[19]. Note that our scintillating probes have already demonstrated their effectiveness in monitoring dwell times ranging from 0.2s to 11s.[30].

II.F.2. Source position monitoring

The instant position of the source at each acquisition time is retrospectively determined from the output signals of the MPD and the source activity using the calibration curves presented in section II.E.. To ensure that the transitory phases between two successive dwell positions are not taken into account in the source tracking, the first and the last signal points for each dwell position are ignored. These transitory phases, which last a few tens of milliseconds[37], correspond to the displacement of the radioactive source between two dwell positions.

During a treatment delivery, each probe j $(1 < j < 7)$ of the MPD delivers a temporal signal $S_j(t)$. At each instant $t = k\tau$, where $k \in \mathbb{N}$ and τ is the acquisition time of the camera, the instant source position is deduced from the readout signal S_j as follows.

First, function f_j^k is defined for each probe j as:

$$f_j^k(z) = \left| C_j(z) - S_j^k \right|, \tag{1}$$

where $C_j(z)$ and S_j^k are the calibration curve and the readout signal of the j^{th} probe at the k^{th} time step, respectively. z corresponds to the spatial coordinate along the axis of the source catheter. Calibration curves being symmetric regarding the z-coordinate, each probe provides two likely instant source positions located on both sides of function f_j^k. Therefore, at minimum two probes are necessary to unambiguously determine the position of a stepping

BT-source.

The instant source position Z^k is determined using four different methods involving various manipulations of functions f_j^k. To find the inter-probe spacing which optimizes source tracking accuracy (for detector design purpose), source position verification is realized from a "two-probe" dosimetry using Eq. 2 ($m = 1$). $j_1 \in [1,6]\backslash 5$ and $j_2 \in [2,7]\backslash 5$ are the indices of the probes forming the 15 probe pairs (j_1,j_2) allowed by our detector. The inter-probe spacing ranges from 5 mm to 52 mm. Probe P5, which is bare to assess in-fiber Cerenkov effect, is not involved in the source position monitoring. Source tracking is systematically analyzed from each of the 15 probe pairs of the detector.

$$Z_m^k(z) = \min\left[f_{j_1}^k(z) + f_{j_2}^k(z)\right], \tag{2}$$

We also tested and compared three different source tracking algorithms. In each case, all the six scintillating probes are involved in the source position monitoring during the treatment delivery. The two first values of the instant source position (Z_m^k, m =2 and 3) are calculated from the readout signals of probe pairs dynamically chosen among the six available probes of the MSD. In both of these two-probe measurements, the source position is defined from Eq. 2 with indices j_1 and j_2 which vary with the source position along (0z). Probe pairs are dynamically chosen to provide the higher readout signals (m=2) or on the basis of a maximum gradient of their calibration curves at the source position (m=3). The last z-coordinate of the source Z_4^k is determined by adding functions f_j^k of all seven probes. We have:

$$Z_4^k(z) = \min\left[\sum_{i=1}^{7} f_j^k(z)\right], \tag{3}$$

II.F.3. Dwell time verification

The monitoring of an HDR-BT treatment is known to produce a staircase temporal signal[14,15,29]. The dwell times of the stepping source, which correspond to the duration of the plateaus in between two successive signal edges, can be simply determined from an edge detection within all readout signals of our MPD system. Our edge detection approach involves function F^k defined as:

$$F^k = \sum_{j=1}^{6} \left(S_j^{k+1} - S_j^k \right), \tag{4}$$

By adding the signal derivatives from all probes, our algorithm is expected to reduce undesired fluctuations in the edge detection function (due to readout noise), as compared to that of a single probe detector.

III. Results

III.A. Detector specification and calibration

The specification of the scintillating probes forming the MPD can be found in Ref.[30]. The linearity coefficient of the probes exceeds 0.999 regardless of the source-probe spacings x. The deviation to repeatability remains below 2% for all values of x. The energy dependence of the fiber probes forming the MPD, referred to as the single-probe MSD, has already been characterized in a past study[30]. Figure 2(b) shows the calibration curves of the MPD acquired at source-probe spacings x of 10, 20 and 30 mm. Six gaussian-like profiles are shown per source-probe inter-catheter spacing (one profile per probe), whose maxima coincide with the probe positions along (0z), as depicted in Fig. 2(a). The SNR of the probes forming the detector varies from 110-140 down to 20-25 at source-probe spacings x of 5.5 mm and 40 mm, respectively.

III.B. Source position monitoring

III.B.1. Optimal probe-to-probe spacing

The aperiodic scintillator array of our MPD enables 15 probe pairs whose inter-probe spacings vary from 5 mm to 52 mm. To identify optimal inter-probe spacings for the future MPD designs, we analyzed the accuracy of the source position verification over these 15 probe pairs, versus the inter-probe distance δz along the detector axis (0z) (see Fig. 3). The instant source position is determined from Z_1^k function, cf. Eq. 2 ($m = 1$). The displacement range of the BT source along (0z) varies with the inter-probe distance δz as $\delta z + 2 * 0.75$ cm (see inset of Fig. 3(b)).

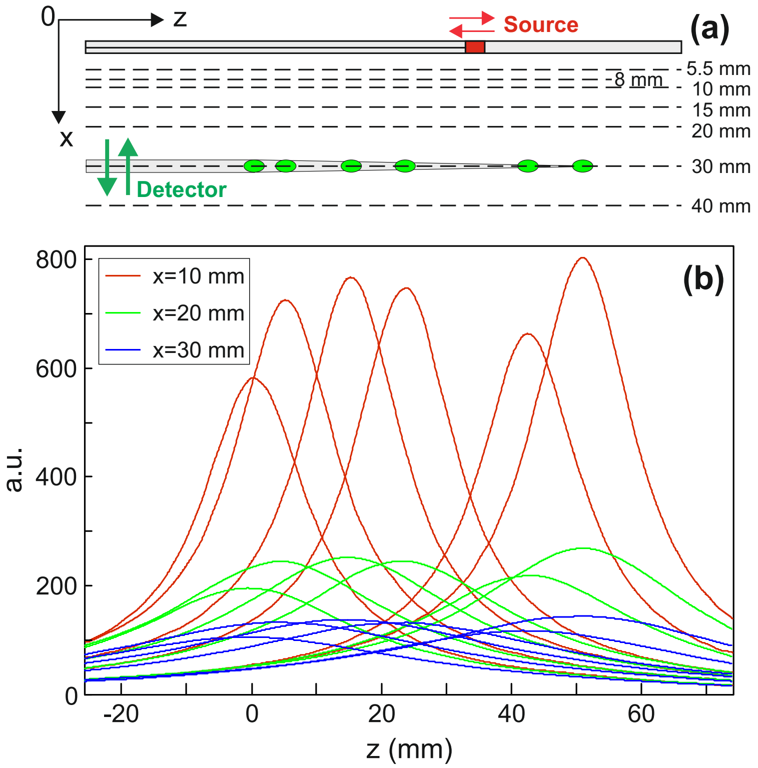

Figure 2: (a) Schematic of the experimental set-up in the water tank. The coordinate frame defining the axis convention is shown in the top-left corner. The source and MPD are represented in red and green, respectively. All seven positions of the MPD defining source-probe spacings x ranging from 5.5 to 40 mm are represented with dashed lines. The source and MPD move along the (0z) and (0x) axes, respectively. (b) Calibration curves of the MPD used for source tracking at x equal to 10, 20 and 30 mm.

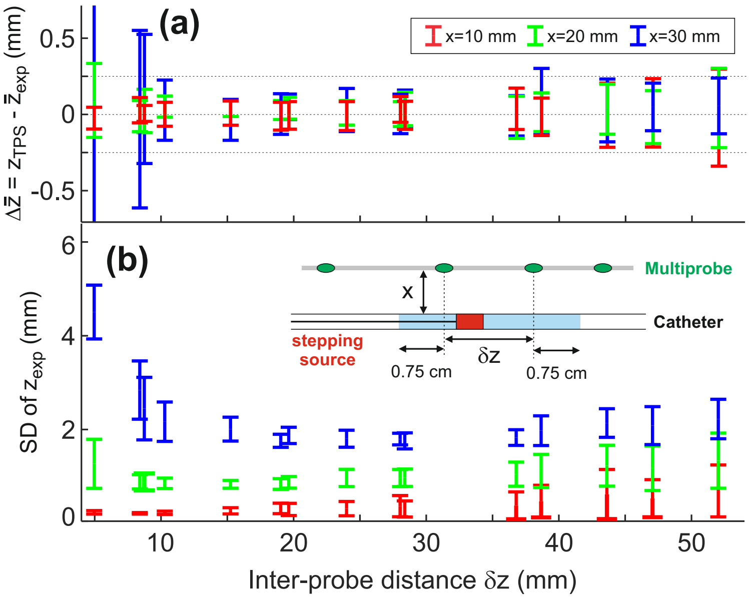

Figure 3: Optimal inter-probe spacing for source tracking. (a) Offset between the measured and planned dwell positions along (0z) ($\bar{z}_{exp}$ and z_{TPS}, respectively) as a function of the inter-probe distance δz. The measured dwell position $\bar{z}_{exp}$ corresponds to the average of the instant source position Z_1^k (see Eq. 2) over a dwell time. Each error bar shows for one source-probe inter-catheter spacing x (see inset of (a)) the offset analysis to the planned dwell positions (mean and standard deviation). This analysis is performed over z-coordinates spanning over $\delta z + 2 * 0.75$ cm (see inset of (b)). (b) SD of the experimentally determined source position Z_1^k versus the inter-probe distance δz. Each error bar shows the distribution (mean and standard deviation) of the SD for dwell positions within $\delta z + 2 * 0.75$ cm (see inset of (b)), at a given source-probe inter-catheter spacing x (see inset of (a)).

We see from Fig. 3(a) that the minimum deviation to the planned dwell positions occurs at δz values in-between 15 mm and 35 mm, regardless of the source-probe inter-catheter spacing x. In that δz range, the offset distribution to the planned dwell positions does not exceed 0.05 ± 0.15 mm at x=30 mm (0.15 ± 0.41 mm at x=40 mm). The SD of the measured instant source position Z_1^k reaches minimum values at δz in between $0.87x$ and x (see Fig. 3(b)). This property, which is observed for all values of x ranging from 5.5 mm to 40 mm, is imputed to the broadening of the calibration curves along (0z) as the source-probe inter-catheter spacing x increases (cf. Fig 2). The tighter distributions of SD are of 0.2 ± 0.022 mm, 0.82 ± 0.12 mm and 1.78 ± 0.12 mm at x =10, 20 and 30 mm, respectively.

III.B.2. Source tracking: two-probe versus all-probe detection strategies

A six-probe detector enables numerous detection strategies for source tracking. In Fig. 4, we compare three algorithms which involve dosimetry either from probe pairs dynamically chosen during the treatment delivery (cf. Z_2^k and Z_3^k of Eq. 2) or from all the probes of the detector (cf. Z_4^k of Eq 3).

At source-probe spacings x below 15 mm, all three source-tracking algorithms show similar accuracy. The mean and standard deviation of the offset to the planned dwell positions do not vary by more than 0.008 and 0.014 mm, respectively, from one method to another (Fig. 4(a)). With the two higher signal method (cf. Z_2^k of Eq. 2), the deviation to the planned dwell positions, which is of 0.007±0.138 mm at x=20 mm, increases up to 0.20 ± 1.12 mm at x= 40 mm. As a comparison, the dwell position verification from the two signals of steeper gradients (calculation of Z_3^k) leads to a mismatch to the treatment plan of 0.027±0.115 mm and -0.11±0.68 mm at x equal to 20 and 40 mm, respectively. Source tracking from all detected signals (calculation of Z_4^k) is much less impacted by the enhancement of the source-probe inter-catheter spacing x. The offset to the planned dwell positions is of 0.029±0.078 mm at x=20 mm and 0.02±0.19 mm at x=40 mm, respectively.

The SD of the instant source position determined from the three above-mentioned methods is reported in Fig. 4(b). For source-probe distances below 15 mm, all three methods determine the instant source positions with almost the same accuracy. When x exceeds 20 mm, the dwell position verification from the two higher detected intensities (calculation of Z_2^k) is the less accurate. A detection from all probes (cf. Z_4^k) minimizes signal fluctuations.

Fig. 5 displays a detailed representation of the source position determined from all scintillating probes, which correspond to the analysis shown in Fig. 4 (cf. black error bars). Fig. 5(a) reports the error to the planned dwell positions, which corresponds to the difference between the planned and measured dwell positions (z_{TPS} and $\bar{z}_{exp}$, respectively). Fig. 5(b) reports the SD of the instant source position Z_4^k, i.e., the SD of the distribution of source positions measured at a rate of 0.06s during a dwell time. Noticeable enhancement of the SD is observed when the source is positioned out of the region where the probes are located, i.e., in between the detector and probe P_1 ($\bar{z}_{exp} < 0$) or beyond probe P_7 ($\bar{z}_{exp} > 5.2$ cm ; cf. Fig. 1(b) and Fig. 2). This local fluctuation enhancement is maximum when x=5.5

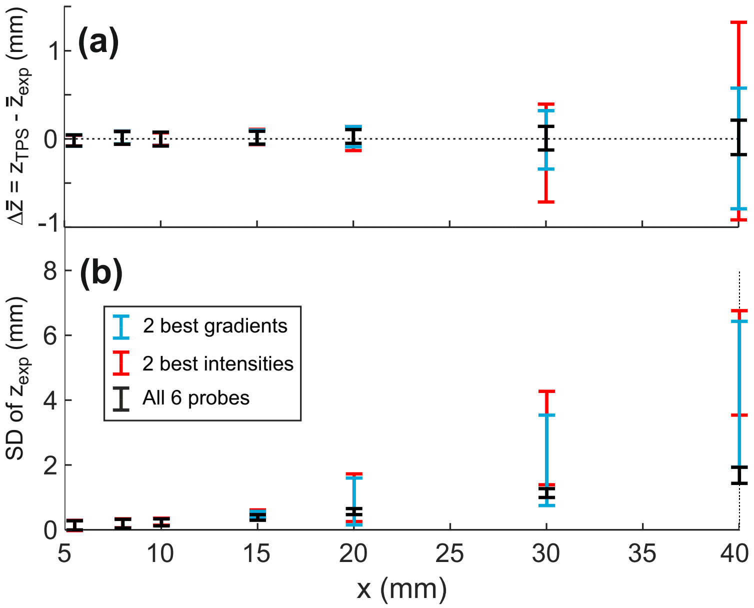

Figure 4: Source tracking: two-probe versus all-probe algorithms. (a) Offset between the measured and planned dwell positions along (0z) ($\bar{z}_{exp}$ and z_{TPS}, respectively) as a function of the source-probe inter-catheter spacing x. The measured dwell position $\bar{z}_{exp}$ corresponds to the average of the instant source position over a dwell time. The instant source position corresponds to Z_2^k, Z_3^k or Z_4^k (cf. Eqs. 3 and 2; see inset of (b)). Each error bar shows for one algorithm (see inset of (b)) the analysis of the offset to the planned dwell positions (mean and SD). This analysis is performed over a range of source positions along (0z) of 10 cm. (b) SD of the experimentally determined instant source positions Z_2^k, Z_3^k and Z_4^k. Each error bar shows for one algorithm (see inset of (b)) the analysis (mean and SD) of the distribution of SD for dwell positions spanning over 10 cm (along (0z)).

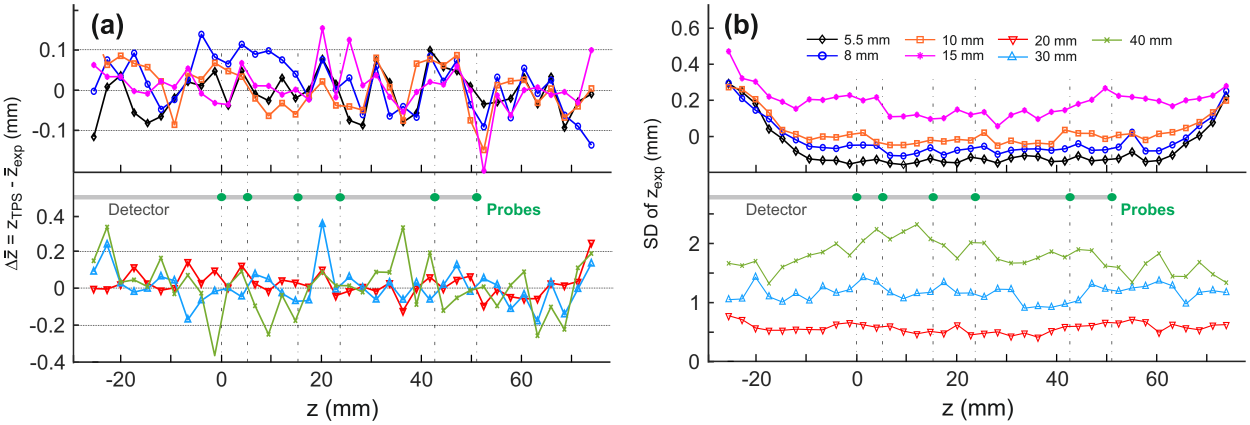

Figure 5: Analysis of an "all-probe" source tracking. (a) Offset between the planned and experimentally determined dwell positions along (0z) (z_{TPS} and $\bar{z}_{exp}$, respectively). $\bar{z}_{exp}$ is the average of the measured instant source position Z_4^k over a dwell time. The mismatch to the planned dwell positions is shown for seven values of the source-probe inter-catheter spacing x (see legend of (b)). (b) SD of the measured instant source position Z_4^k along (0z) as a function of the z-coordinate. Here again, seven source-probe spacings x are considered (see legend). Insets of (a) and (b), schematic of the multiprobe detector which identifies the z-coordinates of the scintillators on the graphs (with dashed lines).

mm and lessens as the source-probe spacing x increases, to finally vanish at x=20 mm. On the contrary, the offset to the planned dwell positions remains at the same level over the entire displacement range of the stepping source (i.e., 10 cm), regardless of the source-probe spacing x (cf. Fig 5(a)).

III.C. Dwell time verification

In Fig. 6, we report the analysis of the offset ΔT between the measured and planned dwell times (T_{exp} and T_{TPS}, respectively) as a function of the source probe inter-catheter spacing x. The error bars show the mean and SD of the offset to the planned dwell times (calculated over 40 dwell positions). The average of ΔT is estimated to be -0.006 ± 0.009 s.

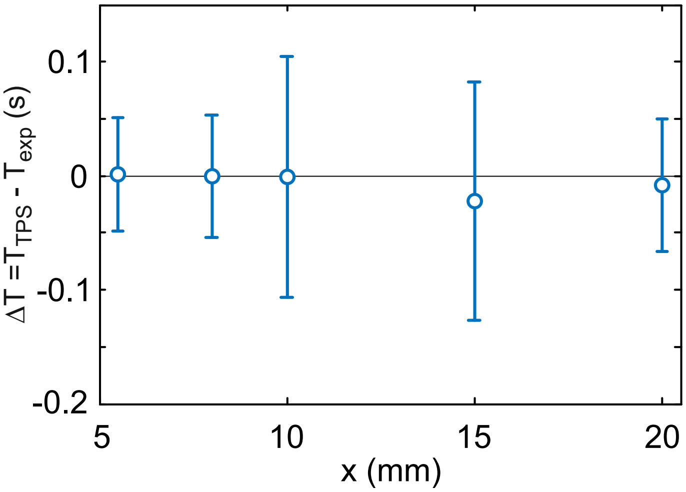

Figure 6: Mismatch ΔT between the measured and planned dwell times (T_{exp} and T_{TPS}, respectively) as a function of the source-probe spacing x.

IV. Discussion

IV.A. Detector specification and calibration

Our MPD shows an acceptable SNR for an accurate dwell time and position verification (larger than 20). At a source probe spacing x of 20 mm, Linares et al. reported a SNR ranging from 13 to 23 with their multipoint detector system involving three photomultiplier tubes (PMT) as photometers[25]. At the same source-probe spacing, we measure a SNR spanning from 33 to 39 with a sCMOS camera, a detection rate of 0.06 s and sensitive volumes that are 250 to 650 times smaller than those of Linares's multipoint detector[25]. SNR could even be enhanced either by slightly broadening the scintillation cell and the fiber core (cf. Ref.[30]) or by replacing the sCMOS camera by six PMTs which provide higher light detection sensitivity and an acceptable detection speed. However, six (or seven) PMTs may be more expensive than a sCMOS camera. Moreover, the performance of these ultrasensitive photometers can be seriously reduced after misuse (such as, e.g., exposing the PMT to room light). Note that the range of SNR observed across the probe array for each source-probe spacing x is due to small discrepancies in scintillation volume and in-fiber luminescence coupling efficiency of the probes. We did not observe noticeable signal variation of the MPD with the slight temperature drift in the water phantom during our experiments, thus confirming the very low sensitivity of the Gd_2O_2S:Tb to changes in temperature[35,36].

Beyond the opportunity of inserting a seven-probe detector within a brachytherapy needle, the advantage of the miniaturization of a water nonequivalent fiber dosimeter resides in a smaller volume averaging effect in the strong dose gradients of the radioactive source, as well as a minimum electron fluence perturbation.

Miniaturization does however not resolve the energy dependence of inorganic scintillator detectors. In contrast to the multipoint detector approach based on organic materials[19,24,25,38], our water non-equivalent multiprobe system requires a space-dependent correction factor for a direct accurate determination of the dose rate at a measured dwell position[30]. To overcome this issue, our strategy is to define a dose rate value from the dwell position and source activity by use of the AAPM TG-43 dose parameters[26]. This indirect dosimetry can be seen to bring the required correction factor[30]. Note that the space-dependent calibration of the organic multipoint detector also relies on the AAPM TG-43 formalism[25].

IV.B. Dwell position verification

IV.B.1. Optimal probe-to-probe spacing

At an interprobe spacing δz of 36.8 mm and at a source-probe spacing x=5.5 mm, our MPD used as a two-probe detector ensures a deviation to the planned dwell positions of 0.03 ± 0.15 mm. We followed the measurement process depicted in Fig. 3(b), with source positions expanding over 51.8 mm along (0z) (i.e., $36.8 + 2 * 7.5$ mm). As a comparison, the deviation to the planned dwell positions is estimated to be 0.45 ± 0.3 mm (1SD) with the three-probe fiber detector of Linares et al[19], at a source-probe spacing $x = 5$ mm and a source activity of 10.73 Ci. Linares's detection system consists of three 10-mm spaced scintillation cells integrated at the end of an individual fiber detection line. Two reasons may explain the higher source-tracking accuracy of our two probe device, despite detection efficiencies of equivalent SNR. First, the sensitive volume of our probes is two orders of magnitude smaller, thereby limiting the averaging effect in the steep dose gradients near an HDR-BT source. Second, the source tracking accuracy of Linares's system may be constrained due to the utilization of non-exclusively experimental calibration, which incorporates the AAPM TG-43 formalism[25].

With a 21-mm spaced four-probe detection system, Guiral et al demonstrated a mismatch to the planned dwell positions of 0.11± 0.7 mm at a 0.1 s detection rate and along a

60 mm portion of source catheter. At a similar source probe spacing estimated to be of 20 mm, we find a deviation to the planned dwell positions of 0.03±0.14 mm over dwell positions expanding over 50 mm. Our sensitive volume being 45 times smaller than Guiral et al.'s[22], volume averaging effect is reduced, thereby improving dwell position verification.

IV.B.2. Source tracking: two-probe versus all-probe detection strategies

Cascading scintillating probes along the source catheter allows for extending optimum source tracking capabilities over longer source paths. The source tracking accuracy reported above can be improved when the probe pair is dynamically chosen among the six available probes of the detector to follow the source during the treatment delivery (all six probes are sequentially involved in the treatment monitoring). The detection accuracy for the "two best gradients" surpass that of the "two best intensities" algorithm. At a 10 s dwell time, source tracking accuracy from these two algorithms is only slightly better than for the fixed two-probe system but the gap should be noticeably enhanced for shorter dwell times, especially the sub-second regime. The two investigated algorithms could also show improved performances if a constant interprobe spacing was considered.

Source tracking accuracy is noticeably enhanced when the source position monitoring is done via the accumulation of all the six readout signals of the detection system. In that case, the deviation to the planned dwell positions is reduced to -0.017±0.063 mm and 0.029±0.078 mm at the source-probe spacings x of 5.5 and 20 mm, respectively. At $x = 5.5$ mm, we observe a maximum offset to the treatment plan of 0.12 mm. As a comparison, Linares et al reported a maximum deviation of 1.8 mm at $x = 5$ mm and at similar source displacement range (10 cm) and dwell time (10s)[19]. At $x = 20$ mm, Guiral et al found a discrepancy to the treatment plan of 0.11± 0.7 mm with their four-probe detection system (at a dwell time of 5s)[22]. The accuracy of the MPD in dwell position verification is fully compatible with the requirements of HDR brachytherapy in terms of medical treatment and quality assurance[1,7,39,40].

Over the entire displacement range of the stepping source (i.e., 10 cm) and at a dwell time of 10 s, the "all-probe" detection approach provides a dwell position verification that is not affected by the fluctuations of the instant source position $\bar{z}_{exp}$, whatever the source-probe spacing x. Although the SD of $\bar{z}_{exp}$ varies by one order of magnitude during the treatment at

$x = 5.5$ mm (Fig. 5(b)), the dwell position measurement remains at the same accuracy level (Fig. 5(a)). The offset to the planned dwell position shows a narrow distribution of 0.002 ± 0.049 mm and a maximum value which does not exceed 0.12 mm. Such performances exceed those of competing multipoint scintillator detectors[19]. Note that all these results are obtained at a noticeably long dwell time. Measurements within a range of shorter dwell times will be studied in the future. A measurement accuracy of 0.023 ± 0.077 mm has already been shown with a single MSD for dwell times ranging from 0.1 to 11 s[30].

IV.C. Dwell time verification

Across the source-probe spacings x ranging from 5.5 to 20 mm, the total average of the differences ΔT between the measured and planned dwell times is of -0.006 ± 0.009 s, at a detection rate of 0.06 s. At $x = 20$ mm, ΔT is found to be -0.008 ± 0.058 s. With their four-probe detector, Guiral et al measured a difference ΔT of 0.05 ± 0.9 s at approximately similar source-probe spacing, a detection rate of 0.1 s and for 5-s dwell times[22]. In their study, the source positions expanded over 6 cm within the source catheter, rather than 10 cm as in our case. At $x = 5.5$ mm, we find an offset ΔT of 0.0009 ± 0.0497 s. As a comparison, Linares et al reported an offset to the planned dwell time of 0.33 ± 0.37 s at $x = 5$ mm and a dwell times of 1s.

It is noteworthy that the measurement errors of the dwell time discussed here are all obtained from an edge detection in a staircase detection signal. In all the proposed methods, dwell times are defined as the elapsed time in between two successive signal edges, which are identified from a signal derivative calculation. Since all the considered dwell times in the above-cited studies are at least 50 fold longer than the integration time of the photometers used, one can assert that the measurement accuracy will not significantly change as the dwell time increases. We recently verified this property in a single probe detection[30]. Therefore, the results from Guiral's and Linares's multiprobe detectors obtained with 5 s and 1 s dwell times, respectively, can be directly compared to our results measured at a dwell time of 10 s. As an example, the lower measurement accuracy of Linares's approach may be partly explained by their shorter 1 mm inter-dwell spacing, leading to noticeably smaller temporal edges (given the strong dose gradients involved), rather than the use of a shorter dwell time of 1s.

Finally, note that the individual component of the MPD, referred to as the single-probe MSD, has already demonstrated its capability in monitoring prostate treatment sequences encompassing dwell times ranging from 0.2 to 11 seconds.[30]. With our probe approach for a MPD, 94% of the 966 dwell positions were successfully identified, with an average deviation to the planned dwell times of 0.005 ± 0.060 and a 100 % detection rate for dwell times exceeding 0.5 s (17%, 86%, 91% and 95% of the dwell times of 0.2 s, 0.3 s, 0.4 s and 0.5 s were successfully identified, respectively).

IV.D. Clinical use

Our multiprobe detector is compatible with clinical applications. It indeed consists of biocompatible elements and it is sufficiently narrow to be inserted in a BT needle or in a catheter. As a preliminary step, we successfully positioned our detector in a one-millimeter wide sealed encapsulation pipe made of PEEK material.

In vivo applications forbid the use of our motorized stage for probe positioning. In gynecologic BT, the probe and the source would be inserted in two parallel catheters of an applicator. The inter-catheter spacing would be precisely known, as in the case of the present study. In prostate BT, the probe and the source are inserted in two independent needles which are implanted manually in a patient. Therefore, x and z coordinates (cf. Fig. 2(a)) are usually coupled since the needles are rarely implanted perfectly parallel from each other, due to operational uncertainties. x and z coordinates of the source relatively to the probe could however be simultaneously determined by various triangulation approaches that would be rendered possible by our six-probe detection system (see for instance Ref.[19]). Source tracking via a triangulation process requires a refined 2D calibration plot of the system, which would not represent a challenge here[30]. Moreover, parallel IVD from a pair of multi-probes detectors connected to the same camera and inserted in two different needles would allow a 3D positioning of the source by triangulation[38] with minimum equipment.

Note that further experiments are required to assess the compatibility of our probe with various clinical scenarios. Firstly, it is necessary to repeat measurements using sources of lower activities, specifically those nearing the end of their clinical lifespan (around 3 or 4 months). This will help evaluate the probe's performance under non-optimum conditions leading to lower SNR. Secondly, it is important to test our fiber detector while it is positioned within a plastic catheter or either a plastic or metallic needle, depending on the specific treatment being targeted. This evaluation will provide insights into the probe's functionality and reliability when used in conjunction with different types of delivery devices potentially attenuating or spectrally modifying radiations at probe locations. Lastly, it is recommended to consider treatment sequences that involve dwell times of fractions of seconds, various source steps (reduced to 1 mm), and source-probe spacings larger than 4 cm. By examining these parameters, we could gain a comprehensive understanding of the probe's performance across a wider range of clinical scenarios.

As mentioned earlier, the individual component of the MPD, specifically the single probe fiber detector, has already been successfully demonstrated in accurately monitoring dwell times down to 0.2 seconds, with source-probe distances of up to 4.7 cm[30]. In cases where the source-probe distance exceeds 4 cm, an alternative multiprobe architecture is envisioned. This architecture would involve multiple MPDs, each incorporating 2 to 4 probes equally spaced apart. These MPDs, inserted within different catheters or needles and engineered from the same fiber bundle, would be positioned parallel to each other, and separated by approximately 3 cm within the treatment volume. This proposed configuration would provide the capability to accurately monitor the source in three dimensions (3D) throughout the larger treatment volumes typically encountered in brachytherapy.

V. Conclusion

We have demonstrated in a water phantom a monitoring device for HDR-BT based on a six-probe scintillator dosimeter coupled to a sCMOS camera. Being engineered at the end of a narrow 270-μm diameter fiber bundle, our miniaturized probes combine high spatial resolution and high detection speed while ensuring a minimum perturbation of the therapeutic process, even if water nonequivalent (inorganic) materials are used. Moreover, the overall dosimeter is totally free from inter-probe cross-talk. The use of a sCMOS camera, rather than seven photomultiplier tubes of higher sensitivity offers the possibility of a simultaneous parallel readout of the six scintillating probe signals, plus the residual Cerenkov signal after chromatic filtering (from the bare fiber), in a simple and low cost architecture that is suitable for clinical use. The lower SNR of the camera is compensated by a higher probe detection efficiency enabled by our concept of an IVD micro-pixel based on a nano-optical interface in between scintillators and a fiber[28].

First, we found a range of probe-to-probe spacings which minimizes source tracking uncertainties. This will be an important information for future MPD designs. We then studied and compared three different source tracking algorithms from the large array of options available within our six-probe system. The best detection approach was found by adding the parallel readout signals from all the probes of the detector. Realizing a source tracking based on this overall accumulated readout signal led to an offset to the planned dwell position as small as 0.01 ± 0.14 mm and 0.02 ± 0.29 mm over a 10-cm long source displacement in the source catheter and at spacings between source and probe catheters of 5.5 and 40 mm, respectively. Using this method, we also measured deviations to the planned dwell time of -0.006±0.009 s and -0.008 ± 0.058 s, at source-probe spacings x of 5.5 mm and 20 mm, respectively (detection rate of 0.6 s). All the studied configurations were found to surpass current fiber-integrated multiprobes and multipoints detection systems. The next steps will be to test our detection system with various treatment plans used for instance in prostate brachytherapy. The detection performances demonstrated here need to be assessed at shorter dwell times down to a fraction of a second. Triangulation approach will also be realized to simultaneously define the dwell time and the 2D coordinates x and z of a stepping HDR-BT source.

Acknowledgments

The authors thank Lionel Pazart, Thomas Lihoreau and Karine Charriere for helpful discussions. This study is funded by the SAYENS Agency, the French Agency of Research (contract ANR-18-CE42-0016), the Region ”Bourgogne Franche-Comte” and the EIPHI Graduate School (contract ANR-17-EURE-0002). This work is supported by the French RENATECH network and its FEMTO-ST technological facility.

References

[1] H. D. Kubo, G. P. Glasgow, T. D. Pethel, B. R. Thomadsen, and J. F. Williamson, High dose-rate brachytherapy treatment delivery: report of the AAPM Radiation Therapy Committee Task Group No. 59, Med. Phys. **25**, 375–403 (1998).

[2] J. Crook, M. Marbán, and D. Batchelar, HDR prostate brachytherapy, in *Semin. Radiat. Oncol.*, volume 30, pages 49–60, Elsevier, 2020.

[3] C. Shah et al., The American Brachytherapy society consensus statement for skin brachytherapy, Brachytherapy **19**, 415–426 (2020).

[4] A. N. Viswanathan, S. Beriwal, F. Jennifer, D. J. Demanes, D. Gaffney, J. Hansen, E. Jones, C. Kirisits, B. Thomadsen, and B. Erickson, American Brachytherapy Society consensus guidelines for locally advanced carcinoma of the cervix. Part II: high-dose-rate brachytherapy, Brachytherapy **11**, 47–52 (2012).

[5] L. A. DeWerd, G. S. Ibbott, A. S. Meigooni, M. G. Mitch, M. J. Rivard, K. E. Stump, B. R. Thomadsen, and J. L. Venselaar, A dosimetric uncertainty analysis for photon-emitting brachytherapy sources: Report of AAPM Task Group No. 138 and GEC-ESTRO, Med. Phys. **38**, 782–801 (2011).

[6] J. Valentin et al., Prevention of high-dose-rate brachytherapy accidents. ICRP Publication 97., Annals of the ICRP **35**, 1–51 (2005).

[7] G. P. Fonseca, J. G. Johansen, R. L. Smith, L. Beaulieu, S. Beddar, G. Kertzscher, F. Verhaegen, and K. Tanderup, In vivo dosimetry in brachytherapy: requirements and future directions for research, development, and clinical practice, Phys. Imag. Radiat. Oncol. **16**, 1–11 (2020).

[8] F. Verhaegen et al., Future directions of in vivo dosimetry for external beam radiotherapy and brachytherapy, Physics and imaging in radiation oncology **16**, 18–19 (2020).

[9] K. Tanderup, S. Beddar, C. E. Andersen, G. Kertzscher, and J. E. Cygler, In vivo dosimetry in brachytherapy, Med. Phys. **40**, 070902 (2013).

[10] J. Lambert, D. McKenzie, S. Law, J. Elsey, and N. Suchowerska, A plastic scintillation dosimeter for high dose rate brachytherapy, Phys. Med. Biol. **51**, 5505 (2006).

[11] J. Lambert, T. Nakano, S. Law, J. Elsey, D. R. McKenzie, and N. Suchowerska, In vivo dosimeters for HDR brachytherapy: a comparison of a diamond detector, MOSFET, TLD, and scintillation detector, Med. Phys **34**, 1759–1765 (2007).

[12] F. Therriault-Proulx, T. M. Briere, F. Mourtada, S. Aubin, S. Beddar, and L. Beaulieu, A phantom study of an in vivo dosimetry system using plastic scintillation detectors for real-time verification of 192Ir HDR brachytherapy, Med. Phys. **38**, 2542–2551 (2011).

[13] C. E. Andersen, S. K. Nielsen, S. Greilich, J. Helt-Hansen, J. C. Lindegaard, and K. Tanderup, Characterization of a fiber-coupled luminescence dosimetry system for online in vivo dose verification during brachytherapy, Med. Phys. **36**, 708–718 (2009).

[14] M. D. Belley, O. Craciunescu, Z. Chang, B. W. Langloss, I. N. Stanton, T. T. Yoshizumi, M. J. Therien, and J. P. Chino, Real-time dose-rate monitoring with gynecologic brachytherapy: Results of an initial clinical trial, Brachytherapy **17**, 1023–1029 (2018).

[15] J. Johansen, G. Kertzscher, E. Jørgensen, S. Rylander, L. Bentzen, S. Hokland, C. S. Søndergaard, A. With, S. Buus, and K. Tanderup, Dwell time verification in brachytherapy based on time resolved in vivo dosimetry, Phys. Med. **60**, 156–161 (2019).

[16] G. Kertzscher, C. E. Andersen, F.-A. Siebert, S. K. Nielsen, J. C. Lindegaard, and K. Tanderup, Identifying afterloading PDR and HDR brachytherapy errors using real-time fiber-coupled Al2O3: C dosimetry and a novel statistical error decision criterion, Radiother. Oncol. **100**, 456–462 (2011).

[17] E. B. Jørgensen, J. G. Johansen, J. Overgaard, D. Piché-Meunier, D. Tho, H. M. Rosales, K. Tanderup, L. Beaulieu, G. Kertzscher, and S. Beddar, A high-Z inorganic scintillator–based detector for time-resolved in vivo dosimetry during brachytherapy, Med. Phys. **48**, 7382–7398 (2021).

[18] J. G. Johansen, S. Rylander, S. Buus, L. Bentzen, S. B. Hokland, C. S. Søndergaard, A. K. M. With, G. Kertzscher, and K. Tanderup, Time-resolved in vivo dosimetry for source tracking in brachytherapy, Brachytherapy **17**, 122–132 (2018).

[19] H. M. Linares Rosales, L. Archambault, S. Beddar, and L. Beaulieu, Dosimetric performance of a multipoint plastic scintillator dosimeter as a tool for real-time source tracking in high dose rate Ir brachytherapy, Med. Phys. **47**, 4477–4490 (2020).

[20] E. B. Jørgensen, G. Kertzscher, S. Buus, L. Bentzen, S. B. Hokland, S. Rylander, K. Tanderup, and J. G. Johansen, Accuracy of an in vivo dosimetry-based source

tracking method for afterloading brachytherapy—A phantom study, Med. Phys. **48**, 2614–2623 (2021).

[21] R. Wang, J. Ribouton, P. Pittet, P. Guiral, P. Jalade, and G.-N. Lu, Implementation of GaN based real-time source position monitoring in HDR brachytherapy, Radiat. Meas. **71**, 293–296 (2014).

[22] P. Guiral, J. Ribouton, P. Jalade, R. Wang, J.-M. Galvan, G.-N. Lu, P. Pittet, A. Rivoire, and L. Gindraux, Design and testing of a phantom and instrumented gynecological applicator based on GaN dosimeter for use in high dose rate brachytherapy quality assurance, Med. Phys. **43**, 5240–5251 (2016).

[23] L. Cartwright, N. Suchowerska, Y. Yin, J. Lambert, M. Haque, and D. McKenzie, Dose mapping of the rectal wall during brachytherapy with an array of scintillation dosimeters, Med. Phys. **37**, 2247–2255 (2010).

[24] F. Therriault-Proulx, S. Beddar, and L. Beaulieu, On the use of a single-fiber multipoint plastic scintillation detector for 192Ir high-dose-rate brachytherapy, Med. Phys. **40**, 062101 (2013).

[25] H. M. Linares Rosales, P. Duguay-Drouin, L. Archambault, S. Beddar, and L. Beaulieu, Optimization of a multipoint plastic scintillator dosimeter for high dose rate brachytherapy, Med. Phys. **46**, 2412–2421 (2019).

[26] J. Perez-Calatayud, F. Ballester, R. K. Das, L. A. DeWerd, G. S. Ibbott, A. S. Meigooni, Z. Ouhib, M. J. Rivard, R. S. Sloboda, and J. F. Williamson, Dose calculation for photon-emitting brachytherapy sources with average energy higher than 50 keV: report of the AAPM and ESTRO, Medical physics **39**, 2904–2929 (2012).

[27] L. Archambault, F. Therriault-Proulx, S. Beddar, and L. Beaulieu, A mathematical formalism for hyperspectral, multipoint plastic scintillation detectors, Physics in Medicine & Biology **57**, 7133 (2012).

[28] M. A. Suarez, T. Lim, L. Robillot, V. Maillot, T. Lihoreau, P. Bontemps, L. Pazart, and T. Grosjean, Miniaturized fiber dosimeter of medical ionizing radiations on a narrow optical fiber, Opt. Express **27**, 35588–35599 (2019).

[29] M. Gonod, C. C. Avila, M. A. Suarez, J. Crouzilles, S. Laskri, J.-F. Vinchant, L. Aubignac, and T. Grosjean, Miniaturized scintillator dosimeter for small field radiation therapy, Phys. Med. Biol. **66**, 115016 (2021).

[30] M. Gonod, M. A. Suarez, C. C. Avila, V. Karakhanyan, C. Eustache, J. Crouzilles, S. Laskri, J.-F. Vinchant, L. Aubignac, and T. Grosjean, Characterization of a miniaturized scintillator detector for time-resolved treatment monitoring in HDR-brachytherapy, Phys. Med. Biol. **67**, 245016 (2022).

[31] J. D. Kraus, R. J. Marhefka, and A. S. Khan, *Antennas and wave propagation*, Tata McGraw-Hill Education, 2006.

[32] Z.Qin, Y.Hu, Y. Ma, W. Zhao, W. Sun, D. Zhang, Z. Chen, and E. Lewis, Embedded structure fiber-optic radiation dosimeter for radiotherapy applications, Opt. Express **24**, 5172–5185 (2016).

[33] Y. Hu, Z. Qin, Y. Ma, W. Zhao, W. Sun, D. Zhang, Z. Chen, B. Wang, H. Tian, and E. Lewis, Characterization of fiber radiation dosimeters with different embedded scintillator materials for radiotherapy applications, Sensors and Actuators A: Physical **269**, 188–195 (2018).

[34] M. Alharbi, S. Gillespie, P. Woulfe, P. McCavana, S. O'Keeffe, and M. Foley, Dosimetric characterization of an inorganic optical fiber sensor for external beam radiation therapy, IEEE Sensors Journal **19**, 2140–2147 (2018).

[35] D. O'Reilly, K. Qayyum, M. Alharbi, and M. Foley, Temperature Dependence of Novel Inorganic Scintillation Detectors, in *2020 IEEE Sensors*, pages 1–4, IEEE, 2020.

[36] O. McLaughlin, M. Martyn, C. Kleefeld, and M. Foley, Investigation of temperature dependence of inorganic scintillators using the HYPERSCINT research platform, Rad. Meas. **164**, 106936 (2023).

[37] G. P. Fonseca, R. S. Viana, M. Podesta, R. A. Rubo, C. P. de Sales, B. Reniers, H. Yoriyaz, and F. Verhaegen, HDR 192Ir source speed measurements using a high speed video camera, Med. Phys. **42**, 412–415 (2015).

[38] H. M. Linares Rosales, J. G. Johansen, G. Kertzscher, K. Tanderup, L. Beaulieu, and S. Beddar, 3D source tracking and error detection in HDR using two independent scintillator dosimetry systems, Med. Phys. **48**, 2095–2107 (2021).

[39] M. J. Rivard, B. M. Coursey, L. A. DeWerd, W. F. Hanson, M. Saiful Huq, G. S. Ibbott, M. G. Mitch, R. Nath, and J. F. Williamson, Update of AAPM Task Group No. 43 Report: A revised AAPM protocol for brachytherapy dose calculations, Med. Phys. **31**, 633–674 (2004).

[40] R. Nath, L. L. Anderson, J. A. Meli, A. J. Olch, J. A. Stitt, and J. F. Williamson, Code of practice for brachytherapy physics: report of the AAPM Radiation Therapy Committee Task Group No. 56, Med. Phys. **24**, 1557–1598 (1997).